



Preparation and characterization of $\text{LiNi}_{0.5}\text{Mn}_{1.5}\text{O}_{4-\delta}$ thin films taking advantage of correlations with powder samples behavior

Liping Wang^{a,b,d}, Hong Li^a, Matthieu Courty^{b,d}, Xuejie Huang^a, Emmanuel Baudrin^{c,d,*}

^a Beijing National Laboratory for Condensed Matter Physics, Institute of Physics, Chinese Academy of Sciences, Beijing 100190, China

^b Laboratoire de Réactivité et Chimie des Solides, CNRS UMR 7314, Université de Picardie Jules Verne, 33 rue Saint Leu, 80039 Amiens Cedex, France

^c Laboratoire des Glucides, CNRS FRE 3517, UFR de Pharmacie, Université de Picardie Jules Verne, 1 rue des Louvels, 80039 Amiens, France

^d Institut de Chimie de Picardie, FR3085 CNRS, Université de Picardie Jules Verne, 33 Rue Saint Leu, 80039 Amiens Cedex, France

HIGHLIGHTS

- Preparation of a high voltage thin films by pulsed laser deposition.
- Fine characterization of the thin films using correlations with the results obtained on powder samples.
- First step towards the evaluation of transport properties in this material.

ARTICLE INFO

Article history:

Received 27 July 2012

Received in revised form

17 October 2012

Accepted 29 October 2012

Available online 16 January 2013

Keywords:

High voltage cathode

Spinel

Thin films

Pulsed laser deposition

Oxygen defect

ABSTRACT

The high voltage spinel $\text{LiNi}_{0.5}\text{Mn}_{1.5}\text{O}_{4-\delta}$ films were obtained by pulsed laser deposition. The effects of oxygen deficiency, annealing treatment, and film thickness on microstructure, morphology and electrochemical properties were investigated. We showed that tuning the oxygen pressure and annealing treatment allows modifying the oxygen film stoichiometry. Trying to determine the oxygen stoichiometry in thin films, a series of oxygen-deficient spinel “ $\text{LiNi}_{0.5}\text{Mn}_{1.5}\text{O}_{4-\delta}$ ” powder samples by quench steps from different temperatures were prepared. It is demonstrated that powders and thin films presenting similar cell parameters, namely related to the oxygen stoichiometry, show similar electrochemical profiles. Meanwhile, the compatibility of electrolyte with substrate and the stability of the target were also investigated.

© 2013 Elsevier B.V. All rights reserved.

1. Introduction

Cathode materials with high gravimetric and volumetric energy densities, high rate performances, excellent cycle retention, low cost and high safety are particularly required for the improvement of present lithium ion batteries [1,2]. The main limitations of such systems are indeed related to the cathodic side of the cells. These last years, high voltage spinel “ $\text{LiNi}_{0.5}\text{Mn}_{1.5}\text{O}_{4-\delta}$ ” has been considered as an interesting candidate due to its high operational voltage at ~ 4.7 V versus Li^+/Li , a lithium storage capacity of 148 mAh g^{-1} and stable structure [3,4].

Two different phases, abusively called polymorphs [5], have been reported for “ $\text{LiNi}_{0.5}\text{Mn}_{1.5}\text{O}_4$ ” [6]. A low temperature ordered structure with $\text{P4}_3\text{32}$ space group can be obtained by synthesis in oxygen atmosphere [7] or post-annealing in air below 700°C [8]. In this structure the Li atoms are located at 8c sites, Ni atoms at 4a sites, Mn atoms at 12d sites, and O atoms at 8c and 24e sites. For synthesis routes employing higher synthesis temperature (over 700°C) a “ $\text{LiNi}_{0.5}\text{Mn}_{1.5}\text{O}_4$ ” phase with Fd-3m structure is obtained [9,10]. This high temperature phase is always accompanied with a rocksalt impurity, which has been attributed either to Ni_xO [3], $\text{Li}_x\text{Ni}_{1-x}\text{O}$ [4], or $(\text{LiNiMn})_x\text{O}$ [11], and concomitant to the presence of oxygen deficiency [11]. A similar oxygen evolution is also observed for another spinel, $\text{Li}_{1\pm y}\text{Mn}_2\text{O}_4$ -type materials, and which occurrence impacts on the charge/discharge voltage profiles and the structural mechanism during cycling [12]. Such an evolution is consistent with a peritectoid phase transition evidenced within this system [5]. These phases thus cannot be reported as polymorphs

* Corresponding author. Laboratoire des Glucides, CNRS FRE 3517, UFR de Pharmacie, Université de Picardie Jules Verne, 1 rue des Louvels, 80039 Amiens, France.
E-mail address: emmanuel.baudrin@u-picardie.fr (E. Baudrin).

since the stoichiometries are different (oxygen vacancies and nickel content lower than 0.5). Within the Fd-3m structure, Ni and Mn atoms are randomly distributed at 16d sites. X-ray diffraction (XRD) does not allow distinguishing these two structures because of the closeness of the Ni and Mn atomic scattering factors. Other techniques such as Neutron diffraction, Raman spectroscopy, Fourier transform infrared spectroscopy (FTIR), Transmission electron microscopy (TEM) and electrochemical voltage profiles have been previously used to discriminate them [5,6,13,14].

In such spinel phases the oxygen deficiency impacts on the capacity fading: namely the higher the oxygen vacancies the higher the capacity fading [10]. This could not be related to kinetic problems since the electronic conductivity of the oxygen deficient high voltage spinel phase with Fd-3m ($10^{-4.5}$ S cm $^{-1}$) is higher than stoichiometric LiNi $_{0.5}$ Mn $_{1.5}$ O $_4$ with P4 $_3$ 32 space group (10^{-7} S cm $^{-1}$) [13] due to the mixed manganese valence (Mn $^{3+}$ /Mn $^{4+}$) in the former phase. Finally, the electrochemical mechanism is different for the two phases with namely a two-phase Li deintercalation process for Fd-3m material while there are two successive two-phase transformations for P4 $_3$ 32 material [5,15]. Besides these subtle differences between the two phases, the high voltage reactivity of these electrode materials brings also the problem of electrolyte reactivity and solid electrolyte interphase (SEI) formation [16,17].

To tackle this system, we decided to follow a thin film approach to be able to form “model phases” which could help to understand both fundamental and applied issues within this high voltage spinel family. Pulsed laser deposition (PLD) technique is a quite simple preparation method which allows controlling different parameters for better understanding electrode materials, as we previously reported for LiFePO $_4$ [18–20], or electrolytes [21]: the film thickness, texturation, composition, films density, etc.. Xia's group reported on the preparation and properties of high voltage spinel “LiNi $_{0.5}$ Mn $_{1.5}$ O $_{4-\delta}$ ” thin films grown using PLD [22–24]. However it is still a difficult task to have clear information on the formed films, such as the oxygen defects and the structure of the thin films. In the present paper, we go further into the investigation of the thin films by controlling the deposition parameters and meanwhile taking advantage of the comparison between “LiNi $_{0.5}$ Mn $_{1.5}$ O $_{4-\delta}$ ” powders and thin films as a way to have better information on the thin films and better understanding of their electrochemical behavior.

2. Experimental

2.1. Synthesis of the powder samples

The “LiNi $_{0.5}$ Mn $_{1.5}$ O $_4$ ” samples were prepared by a ceramic route. Typically, stoichiometric amounts of LiNO $_3$, Mn(NO $_3$) $_2$ ·4H $_2$ O, Ni(NO $_3$) $_2$ ·6H $_2$ O were first dissolved in alcohol. Subsequently, the solvent was evaporated under continuous stirring at 80 °C to give thick slurry. This precursor was then smoothly decomposed at 500 °C for 2 h, and further heated at 800 °C for 8 h to ensure complete reaction. Afterward, the furnace was turn off, and the sample let cooled down naturally (cooling rate at around 5 °C min $^{-1}$) towards ambient temperature. Several samples were obtained by first annealing this cooled sample in air at different temperatures (650 °C, 800 °C, 850 °C, 900 °C) for 2 h, followed by a quenching in liquid nitrogen. Samples cooled down naturally from 800 °C, quenched at 650 °C, 800 °C, 850 °C, and 900 °C were denoted C800, Q650, Q800, Q850 and Q900, respectively.

2.2. Thin films preparation

The thin films were grown by PLD. The target, prepared from the C800 sample, was made denser by isostatic pressing at 2000 bar for 25 min followed by an annealing treatment at 600 °C for 48 h in air.

The target density was about 60% of the theoretical one. A KrF laser beam ($\lambda = 248$ nm) with 160 mJ laser energy and 5 Hz frequency was used for the deposition. The film was deposited on Si, Pt, and mirror-like quality polished stainless steel 304 (SS304) substrates. Thin films on Si substrates were only used for estimating the film thickness. Unless otherwise specified, the thickness was about 300–500 nm.

2.3. Characterization

The structure was analyzed using a Bruker D8 Diffractometer equipped with Cu K α ($\lambda = 1.54056$ Å) anticathode. Cell parameters were determined in a pattern matching mode using FullProf (Windows version, March 2007) [25] using the pseudo-Voigt profile function of Thomson et al. [26]. Scanning electron microscope (FEI QUANTA 200 FEG) was used to characterize the surface morphology. Thermogravimetric Analysis (TGA) was performed on a Netzsch thermal analyzer STA 449C Jupiter equipped with a Differential analysis microbalance. The samples (10–15 mg) were heated, in an alumina crucible, under air from RT to 1000 °C with a heating rate of 5 °C min $^{-1}$. Electrochemical characterization was performed using 2032-type coin cells. “LiNi $_{0.5}$ Mn $_{1.5}$ O $_{4-\delta}$ ” was used as the working electrode and lithium foils were used both as counter and reference electrodes. The electrolyte, commercial name LP30, was 1 M LiPF $_6$ in ethylene carbonate (EC) and dimethyl carbonate (DMC) with a volume ratio of 1:1. Cells were assembled in an Ar filled glove box. Galvanostatic charge–discharge tests were carried out at room temperature on VMP3 system (Biologic S.A., Claix, France) from 3.5 to 4.9 V with a constant current of 30 mA g $^{-1}$ for powder electrodes and of 20 μ A cm $^{-2}$ for thin film electrodes.

3. Results and discussion

3.1. Structure and morphology

We firstly examined the structural evolution of the XRD powder patterns for the samples quenched from various temperatures (Fig. 1). The Bragg peaks for the samples quenched at higher temperature shifted to lower angles. Such an evolution is nested in the increase of the cell parameters as the oxygen content evolves (Figure S1). Indeed, the samples quenched at higher temperature are oxygen deficient [11] leading to the partial reduction of manganese from Mn $^{4+}$ to Mn $^{3+}$ (the ionic radius are 0.53 Å and 0.645 Å,

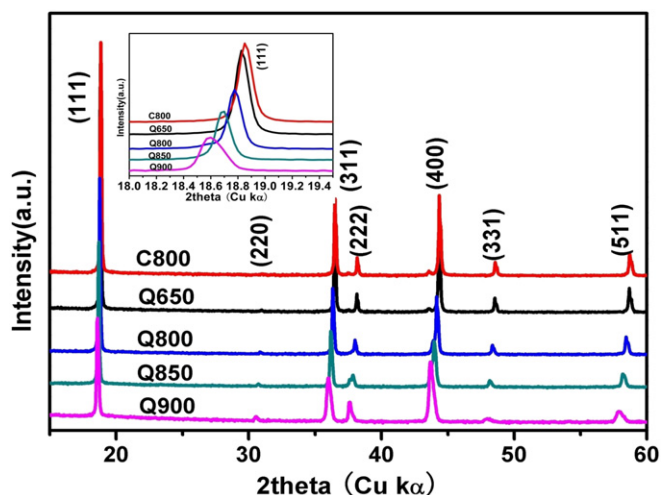


Fig. 1. XRD patterns of “LiMn $_{1.5}$ Ni $_{0.5}$ O $_{4-\delta}$ ” powder samples prepared by quenching C800 samples annealed at different temperatures for 2 h.

respectively [27]). Similarly, the evolution of the spinel cationic stoichiometry due to the peritectoid formation of a rocksalt impurity will also induce an increase of the cell parameters.

As the annealing temperature is increased, we can notice the appearance of the (220) Bragg peak (located at $2\theta = \sim 30.7^\circ$) which reveals the presence of transition metal on supposed Li site. This can be also underlined through the examination of the intensities ratios of the (311) to (111) Bragg peaks which are an indication of the degree of cationic mixing, namely the ratio should increase with increasing cationic mixing [28]. From the XRD patterns of the different samples (Fig. 1), the (311)/(111) intensities ratios are 0.331, 0.339, 0.341, 0.359 and 0.361, for the C800, Q650, Q800, Q850, and Q900 samples, respectively. This demonstrates clearly that the amount of transition metal in the tetrahedral site increases with the elevation of annealing temperature. In short, samples quenched at higher temperature have larger cell parameters and more transition metal on Li site.

To quantify the oxygen non-stoichiometry, we performed thermogravimetric measurements (Fig. 2). For all samples, there is an initial weight gain on the TG curves occurring from $\sim 400^\circ\text{C}$ up to 650°C , while above 650°C we can notice a weight decrease characteristic of oxygen loss. This loss is similar for all samples. As an example, in the inset, we represented the weight evolution during the heating/cooling cycle for sample Q900, which is a sample annealed at 900°C then quenched. Such curve shows that heating this sample leads to a reincorporation of oxygen between 350 and 650°C . This reversibility underlined that the weight evolution is only due to oxygen loss/gain and that lithium oxide loss is insignificant under the used conditions. By assuming that the composition obtained at the maximum weight on the TG curve is $\text{LiNi}_{0.5}\text{Mn}_{1.5}\text{O}_4$, we can estimate the oxygen content of these samples to 3.997, 3.998, 3.934, 3.911 and 3.879 for C800, Q650, Q800, Q850, and Q900, respectively. The evolution of the lattice parameters can thus be correlated with the evolution of the oxygen content of the powder samples (Fig. 3). As we will see below, we will use this plot to have more information on the thin films oxygen stoichiometries.

For the thin film preparation, we used classical deposition parameters for such spinel phases, namely a temperature of 600°C , a 160 mJ laser energy and a 5 Hz frequency. We played mainly on the oxygen partial pressures within the 10–50 Pa range. The films prepared on SS304 substrates are well crystallized (Fig. 4) and we can notice a clear evolution of the peaks position as a function of the deposition oxygen pressure. As compared to the 8.17 \AA cell

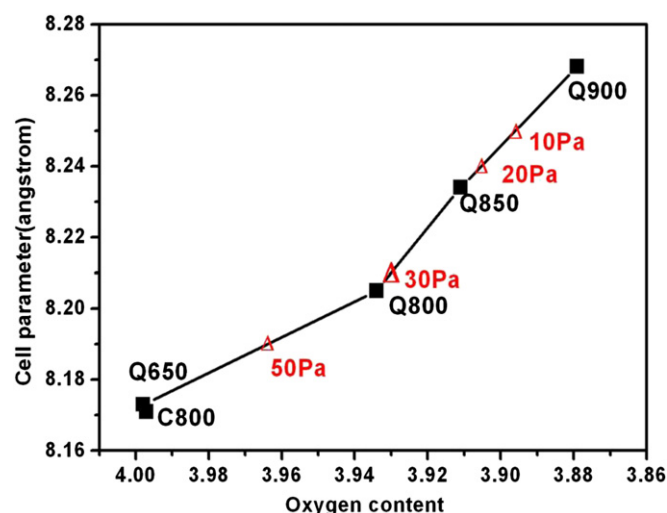


Fig. 3. Lattice parameters evolution of the powders and films with the oxygen stoichiometry for “ $\text{LiNi}_{0.5}\text{Mn}_{1.5}\text{O}_{4-\delta}$ ” samples.

parameter of the used target, the calculated cell parameters of the thin films deposited at 10 Pa, 20 Pa, 30 Pa, and 50 Pa, are 8.25 \AA , 8.24 \AA , 8.21 \AA , and 8.19 \AA , respectively (Figure S2). The (311)/(111) peaks intensities ratio is increasing as the pressure decreases, meaning either there is a texturation along the [311] direction when the pressure is decreased or there is more transition metal ions at the tetrahedral Li site. This latter explanation is the more credible since in general, for spinel phases, preferred orientation occurs along the [111] direction and it is also in good correlation with the observed behavior of powder samples. For the lowest pressure, namely 10 Pa, an extra diffraction peak at about $\sim 43.5^\circ$, which may be attributed to a rocksalt phase, is evidenced (Fig. 4). All the other films correspond to pure spinel phases according to the XRD patterns. The crystallite sizes determined from the half width along the (111) peaks are about 28 nm, 30 nm, 32 nm, and 33 nm for a deposition under 10 Pa, 20 Pa, 30 Pa, and 50 Pa oxygen, respectively. Using a higher oxygen pressure thus leads to a better crystallinity. The corresponding SEM images of the films deposited at different oxygen partial pressures are shown in Fig. 5. It can be seen that pressure plays an important role on morphology. At 10 Pa, the thin film exhibits a very dense and flat surface but with grains

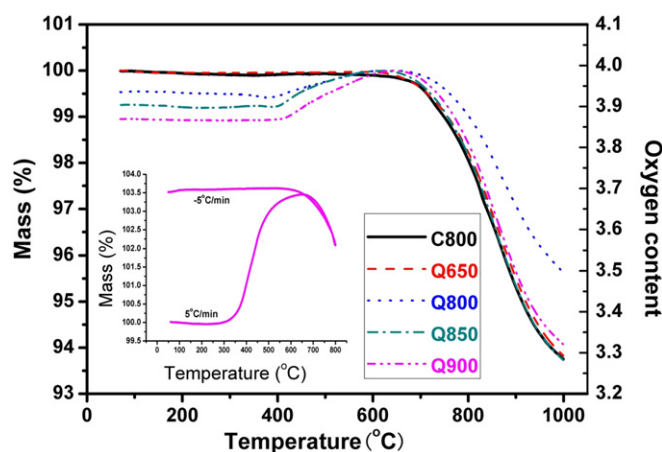


Fig. 2. TG curves in air of various “ $\text{LiNi}_{0.5}\text{Mn}_{1.5}\text{O}_{4-\delta}$ ” samples. The inset graph shows heat/cool curves of sample quenched at 900°C .

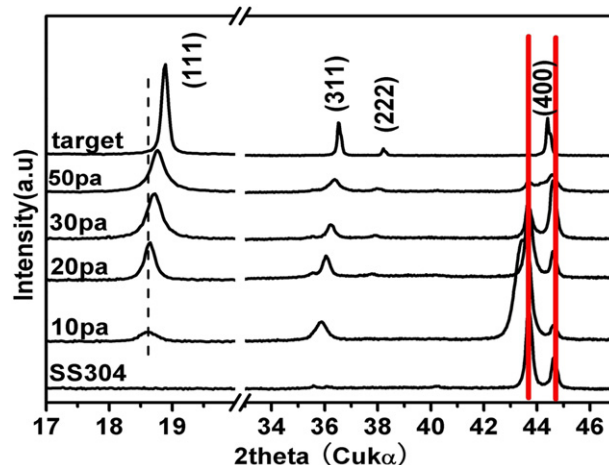


Fig. 4. XRD spectra of the $\text{LiNi}_{0.5}\text{Mn}_{1.5}\text{O}_4$ target and thin films deposited on SS304 at different pressures ($T_s = 600^\circ\text{C}$).

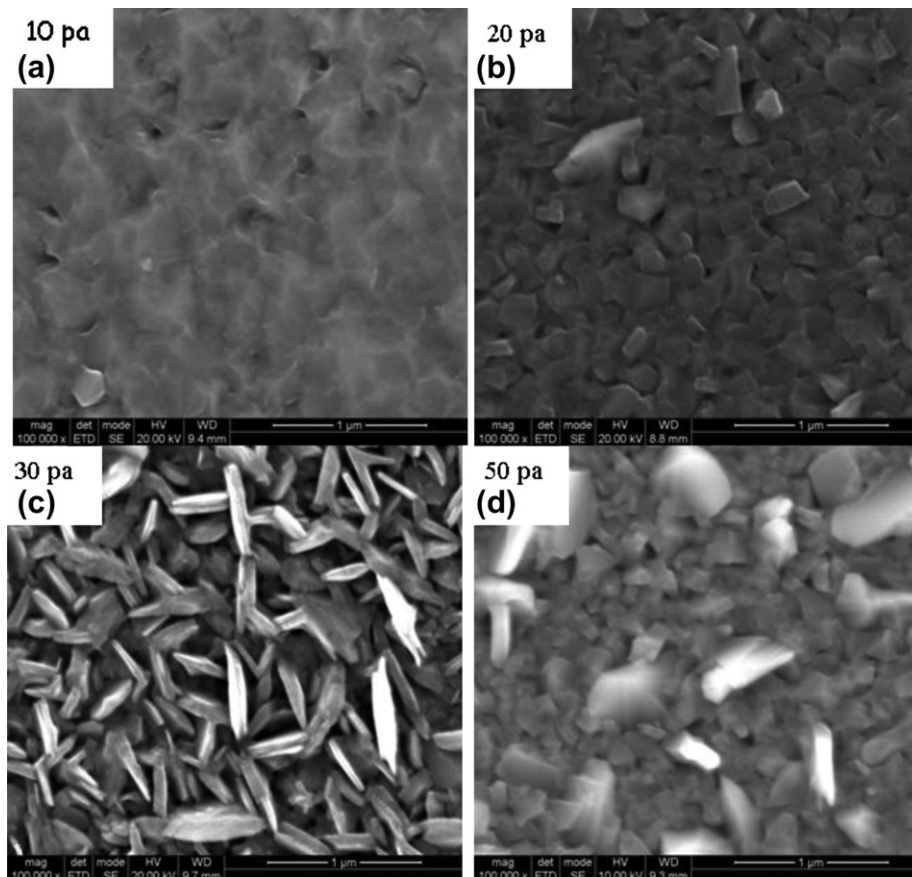
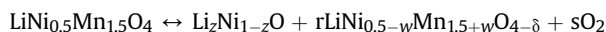


Fig. 5. SEM micrographs of thin films deposited at various oxygen partial pressures ($T_s = 600^\circ\text{C}$): (a) 10 Pa, (b) 20 Pa, (c) 30 Pa, and (d) 50 Pa.

that are not well defined. At 20 Pa, large particles are formed leading to a rough surface. At 30 Pa, a lot of plate-shaped particles are formed, which means the roughness is further increased. At 50 Pa, most of the particles disappeared, and the film has a basis closed to the one of the thin film deposited at 20 Pa onto which a few larger particles are deposited. In general, increasing oxygen partial pressure will lead to structure evolution with namely cell parameters evolution, transition metal on Li site and result in different morphologies with various densities and surface areas. To obtain a good control of the film formation, it is also important to be able to use a reproducible target from which the congruent transfer of matter has to be performed for film formation. The target XRD patterns were acquired before and after a deposition process (Fig. 6). There is a clear evolution illustrated by the decrease in the (111) reflection intensity and the appearance of a rocksalt phase (possibly the generally reported $\text{Li}_x\text{Ni}_{1-x}\text{O}$, Ni_xO , or $\text{Ni}_x\text{Mn}_y\text{O}$) at Bragg angle $\sim 37.5^\circ$, $\sim 43.5^\circ$, and some extra peaks, for instance, at $\sim 18.5^\circ$. This can be partly explained by the peritectoid reaction we proposed previously [5]:



During the plasma formation, the pressure within the PLD chamber is low and the oxygen is “pumped away”, displacing the equilibrium towards the formation of an oxygen under-stoichiometric target containing a rocksalt phase on the surface. The target thus needs to be recovered for a reproducible use. From experience, a simple polishing process using a sand paper allows getting back the pristine XRD pattern and obtaining reproducible deposition (Fig. 6c). Meanwhile, it is necessary to address that in

order to obtain proper and conclusive results concerning the screening of different parameters or to control the phases, we worked on sample batches prepared within a short period in a fixed chamber.

Using thin films is sometime frustrating since it is difficult to characterize them in terms of stoichiometry. Thus, comparing thin films and oxygen-defect powders results are not easy tasks. However, we can take here the advantage of the correlation between the

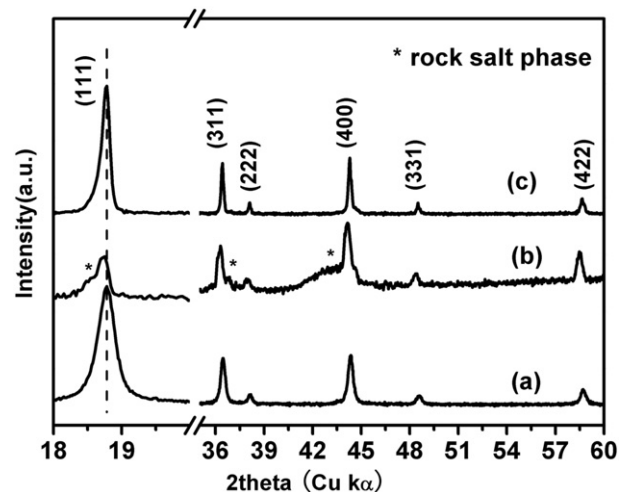


Fig. 6. XRD patterns of target (a) original one, (b) after deposition (*rocksalt phase), and (c) after polishing.

Table 1

Oxygen content of thin films determined from the comparison with powder samples (cell parameters vs. oxygen content) based on Fig. 3.

Sample	Cell lattice (Å)	Oxygen content
10 Pa	8.25	3.896
20 Pa	8.24	3.905
30 Pa	8.21	3.930
50 Pa	8.19	3.965

cell parameters and the oxygen deficiency determined from the powders to evaluate the oxygen stoichiometry of thin films. We thus reported the cell parameters determined for the thin films on the graph gathering the powder samples results (Fig. 3). As we have a continuous increase in the cell parameter for the powder samples, we assume that for similar cell parameters, the thin films will have a close stoichiometry. The obtained values for the different thin films are gathered in Table 1.

In the previous paragraphs we underlined the importance of controlling the oxygen stoichiometry. We further tried to modify it through an annealing treatment in air (thus out of the PLD chamber) at 600 °C for 40 min. Fig. 7 illustrates the XRD patterns of a thin film obtained by *in situ* deposition at 600 °C 50 Pa (denoted as “*In situ* 600”) and a thin film deposited at room temperature, 50 Pa first then post-annealed in air at 600 °C (denoted as “Annealed 600”) on Pt substrates. These two films present different cell parameters as evidenced by the larger diffraction angle for “Annealed 600” ($a = 8.17$ Å) compared with “*In situ* 600” ($a = 8.18$ Å). This means that the annealing treatment, *in situ* vs. *ex situ*, has an influence on the properties of the obtained films. The crystallites sizes are also different: 51 nm for “*In situ* 600” sample and 12 nm for the “Annealed 600” one. The latter sample presents agglomerated particles with a smooth surface but showing typical cracks of post-annealed PLD thin films. On the other hand, the “*In situ* 600” sample displays big particles with a rougher surface.

Finally, for thin films, the thickness can be an important parameter impacting on the properties, especially if some transport limitations are expected. We examined if this was important for the high voltage spinel through the preparation of a panel of samples by simply playing on the PLD deposition time. The thin films presenting different thicknesses (350 nm, 780 nm, and 1100 nm) were thus prepared for a deposition of 20 min, 40 min, and 60 min, respectively (Fig. 8). There is no notable Bragg angle shift on the XRD patterns. The cell parameters are about 8.18 Å with crystallite

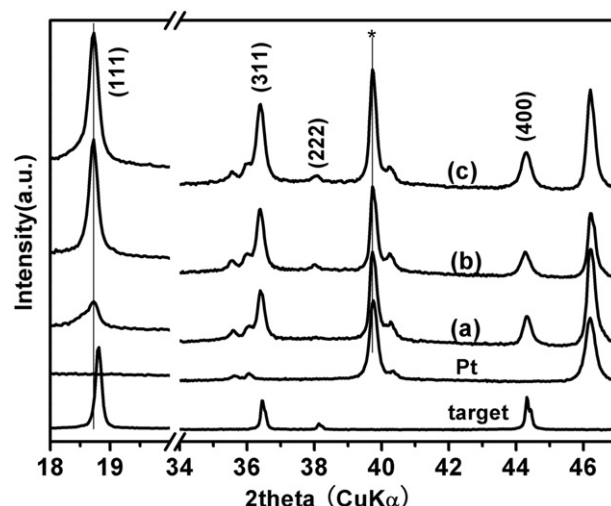


Fig. 8. XRD patterns of thin films with different thicknesses (a) 350 nm, (b) 780 nm, and (c) 1100 nm.

sizes of about 31 nm, 58 nm, and 76 nm, respectively. We thus underline that a constant stoichiometry was obtained whatever the deposition time/thickness.

3.2. Electrochemical performance

The typical charge–discharge curves and cycle performances of powder samples with different oxygen stoichiometries are shown in Fig. 9. There is a small capacity at ~4.0 V, which can be attributed to the $\text{Mn}^{3+/4+}$ redox couple and is related to oxygen non-stoichiometry [6]. For sample C800, at around 4.7 V, two electrochemical phenomena are observed. The first is a quasi-plateau corresponding to the oxidation of Ni^{2+} , through a solid solution mechanism [14]. Then, a flat plateau is formed at 4.76 V. This is a typical two-phase reaction during the oxidation of Ni^{3+} into Ni^{4+} . This is in agreement with the *ex situ* XRD result obtained by Kim et al. [6]. The presence of these two peaks at 4.70 V and 4.76 V is a typical signature of the Fd-3m structure and can thus be used to discriminate between the Fd-3m and P4_332 space groups, the latter reacting electrochemically at 4.66 V and 4.70 V. For sample Q800, Q850, Q900 with severe oxygen deficiency, there is no real plateau,

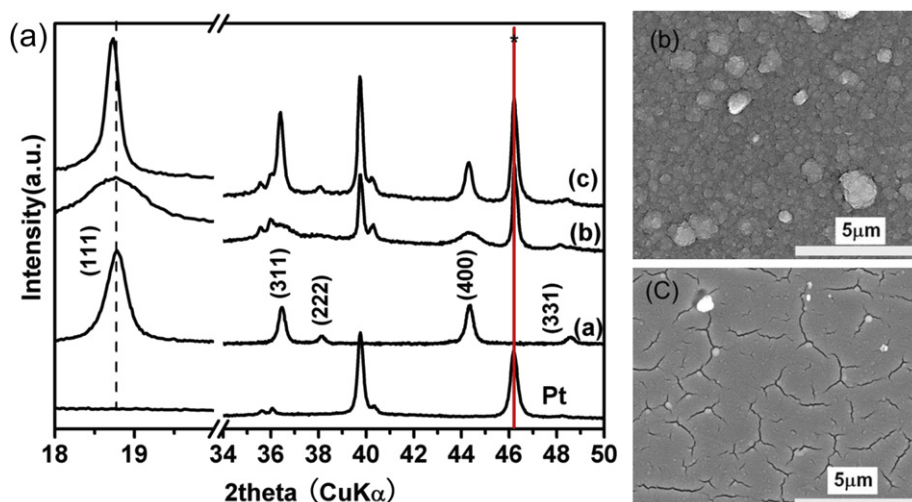


Fig. 7. XRD patterns of (a) target, (b) thin film deposited at room temperature, 50 Pa then anneal in air at 600 °C, and (c) thin film deposited at 600 °C, 50 Pa.

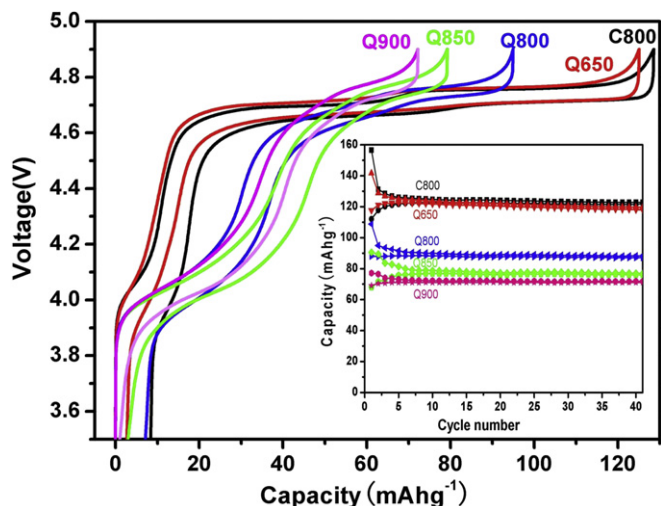


Fig. 9. Charge and discharge curves of various powder samples (inset graph is capacity retention behavior).

but a quasi-plateau behavior. Obviously, samples with more oxygen non-stoichiometry accompanied with more impurity have less capacity. The discharge capacity of samples C800, Q650, Q800, Q850, and Q900 are ~ 125 , 120 , 90 , 80 , and 75 mAh g^{-1} , respectively. Their initial coulombic efficiency is between 71% and 89%, and then increased to 99% after a few cycles. The low coulombic efficiency probably stemmed from the activation of the structure, the electrolyte decomposition at high voltage and/or the formation of SEI.

Compatibility between lithium-based electrolytes and the substrates is very important especially for high voltage thin film electrodes. Fig. 10 reflects the galvanostatic curves using substrates SS304 and Pt. Both SS304 and Pt were treated in deposition chamber at 600°C , 50 Pa O_2 ambient for 40 min to be consistent with thin film deposition process. There are electrochemical reactions between the heated SS304 and electrolyte during the first cycle at $\sim 3.4 \text{ V}$ and $\sim 4.1 \text{ V}$ vs. Li^+/Li . This can be due to the oxidation of SS304 under higher temperature and oxygen atmosphere, this new formed material then reacting electrochemically with the electrolyte. However, the reaction is irreversible as revealed from the first discharge curves. For the Pt, although a pseudo-plateau on charging was observed in the region of $4.5\text{--}4.9 \text{ V}$, the capacity rooted from the

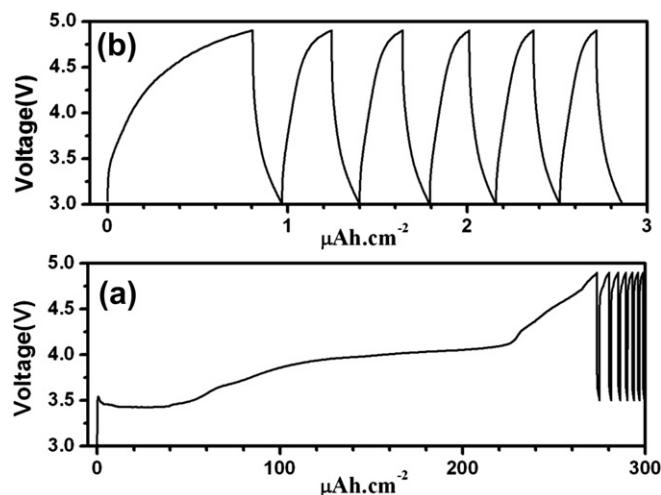


Fig. 10. Galvanostatic curves for substrate/electrolyte/Li cells: (a) SS304 and (b) Pt.

substrate is marginal. The Pt seems suitable for the study of high voltage cathode material.

Fig. 11 reflects the electrochemical behavior of thin films prepared under different oxygen pressures with typical galvanostatic charge–discharge curves (Fig. 11a). These curves have also been normalized to the 100% capacity for an easier comparison (inset graph in Fig. 11a). Under lowest oxygen pressures, all of the samples show a sloppy voltage evolution instead of a plateau expected at $\sim 4.78 \text{ V}$ vs. Li^+/Li . This is inline with the fact that the prepared films are oxygen deficient. When decreasing the oxygen pressure during the deposition, namely increasing oxygen non-stoichiometry δ , the capacity at 4.64 V decreases concomitantly with a capacity increase in the 4 V region that is related to the $\text{Mn}^{3+}/4+$ redox couple. Fig. 11b shows the evolution of the charge and discharge capacities during cycling. For the first few cycles, the coulombic efficiencies are quite low but better capacity retention is obtained for the subsequent cycles powder samples. The sample prepared at 50 Pa presents the best capacity retention reflecting the highest coulombic efficiency. This is most likely linked to both the better crystallinity and the morphology with a lower contact surface area with the electrolyte thus minimizing the dissolution of transition metals.

To add an element showing that the assumption using powder samples to estimate thin films oxygen content does not come out of

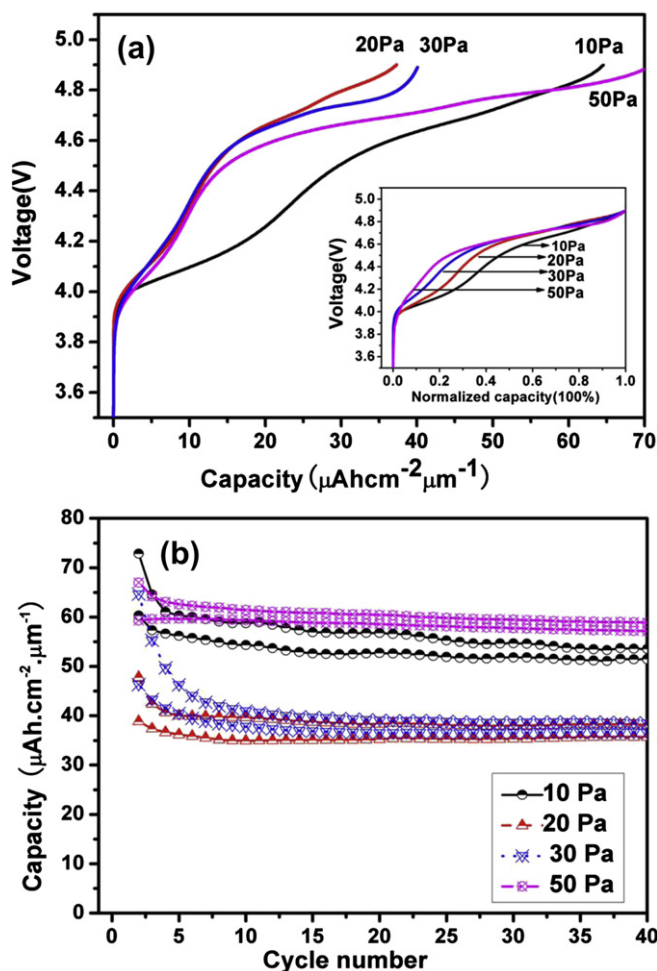


Fig. 11. Electrochemical performance of “ $\text{LiNi}_{0.5}\text{Mn}_{1.5}\text{O}_4$ ” thin films deposited on SS304 under various oxygen partial pressures between 3.5 and 4.9 V at a current rate of $20 \mu\text{A cm}^{-2}$: (a) galvanostatic charge curves at the second cycle for thin film obtained at different oxygen partial pressures, inset graph shows normalized charge curves, and (b) cycling performances from the second cycle.

the blue, we compared the electrochemical properties of thin film/powders with similar cell parameters, and thus similar oxygen stoichiometries (Fig. 12). The selected samples are the thin film deposited at 20 Pa ($a = 8.24 \text{ \AA}$) which is compared with powder sample Q850 and the thin film deposited at 30 Pa ($a = 8.21 \text{ \AA}$) vs. powder sample Q800. It is clear that these samples compare well in terms of capacity and polarization. In other words, the oxygen stoichiometry is a key parameter which governs the electrochemical response.

Fig. 13a illustrates the initial galvanostatic charge–discharge curves for thin films with different thicknesses. The coulombic efficiencies of the first cycle are 41%, 51%, and 57% for films with thicknesses of 350 nm, 780 nm, and 1100 nm, respectively. As mentioned above, the low coulombic efficiency probably stemmed from the electrolyte decomposition at high voltage and/or the formation of an SEI. Thicker film expresses a higher coulombic efficiency, which can be ascribed to the relative less portion of active material contact with electrolyte. This indicates that the attempts to coat such films to hinder the active material contact with electrolyte so as to improve electrochemical performance should be one solution to minimize the irreversible capacity at the first few cycles. Fig. 13b shows the charge–discharge capacity performance as a function of cycle number. The decrease in the capacity for the thicker films is most likely a sign of limitation either in the electronic or ionic transport within the film.

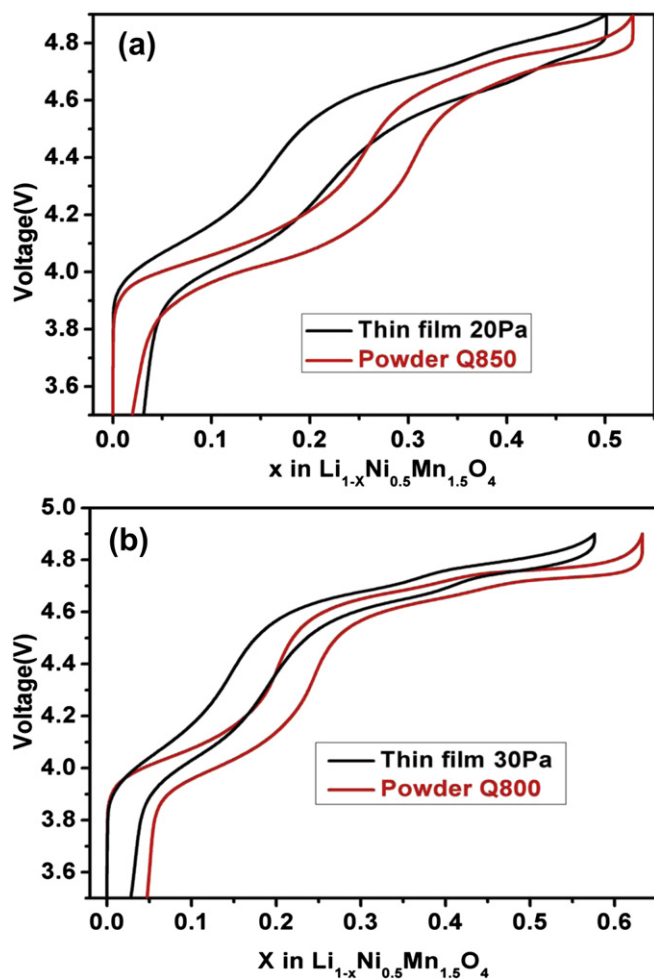


Fig. 12. Comparison of the electrochemical signatures of powder and thin film “ $\text{LiNi}_{0.5}\text{Mn}_{1.5}\text{O}_4$ ” samples with similar cell parameters obtained in a galvanostatic mode.

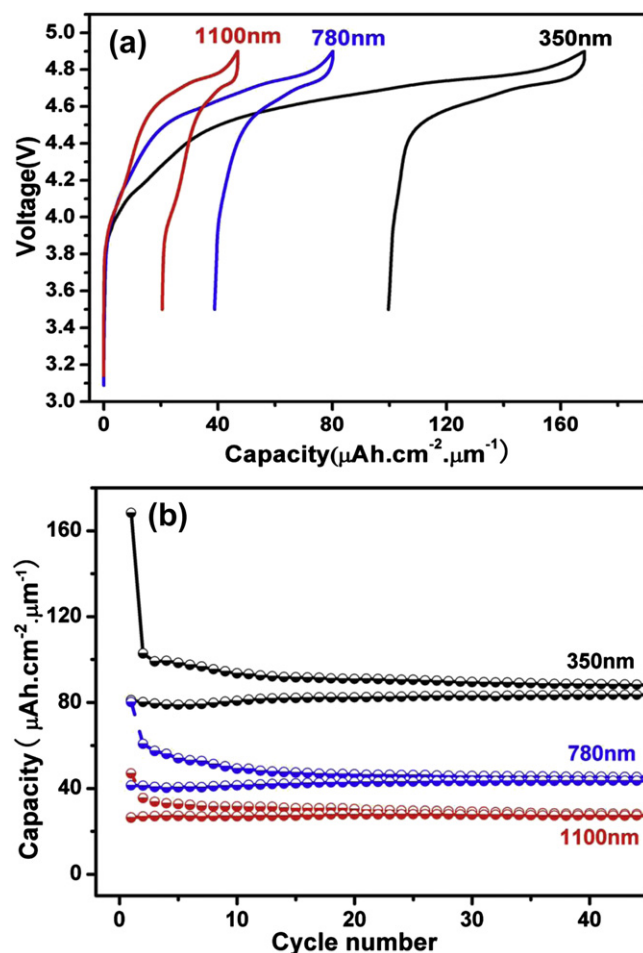


Fig. 13. Electrochemical performance of thin film with different thicknesses: (a) initial galvanostatic charge–discharge curves and (b) cycle performance.

Fig. 14 clearly shows the importance of the annealing process on the electrochemical properties of sample “Annealed 600”. First, the post-annealing process in air enables to integrate oxygen towards a “normal” spinel stoichiometry. This is seen through the important decrease in the amount of capacity observed at about 4.0 V on the electrochemical curve. Furthermore, the thermal treatment leads to

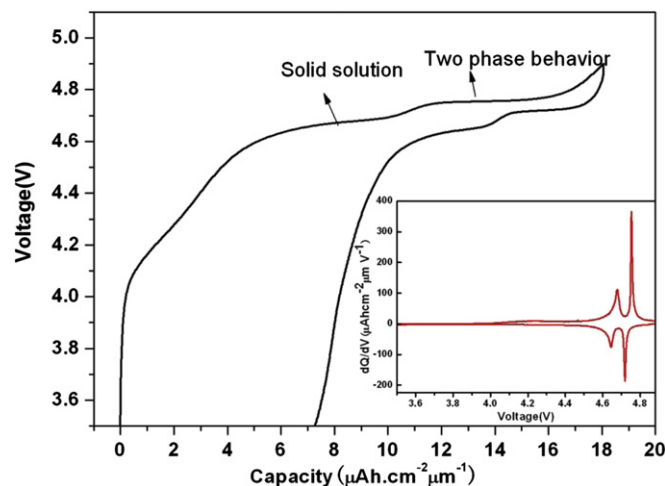


Fig. 14. Galvanostatic signature of thin film “Annealed 600” obtained after a post-annealing treatment of a sample deposited at room temperature under 50 Pa oxygen.

better defined plateaus at 4.68 V and 4.76 V, which are typical of the Fd-3m space group [5]. Although there is an evolution of the electrochemical signature, the charge–discharge capacity is no more than half of the theoretical capacity for a thickness of about 300 nm. We can infer that the low capacity is due to the density of the thin films which do not favor to lithium diffusion.

4. Conclusions

The high voltage spinel films were deposited by pulsed laser deposition on Pt and SS304 which are compatible with the LP30 electrolyte. The effects of deposition pressure and deposition time on microstructure, morphology and electrochemical properties were investigated. The samples deposited at 600 °C under 50 Pa O₂ shows a (111) preferential orientation and high crystallinity. These films demonstrate the best electrochemical performance. We also underlined that playing with the oxygen pressure allows modifying the oxygen film stoichiometry. Furthermore, we showed that the stoichiometry of the films can be evaluated through the determination of the cell parameters of the spinel phase. Indeed, comparing powder with thin films samples we obtained similar charge–discharge curves and capacities for samples presenting similar cell parameters. Another way to control the stoichiometry of the film is to perform a post-annealing in air for samples deposited at RT. The formation of such controlled films could now be used to determine either the physical properties of lithium extracted high voltage spinels or the evolution of the film/electrolyte interface.

Acknowledgements

Financial supports from “973” project (2007CB936501), CAS project (KJCX2-YW-W26) and NSFC project (50730005) are acknowledged. Liping Wang thanks French Government for PhD Scholarship.

Appendix A. Supplementary data

Supplementary data related to this article can be found at <http://dx.doi.org/10.1016/j.jpowsour.2012.10.099>.

References

- [1] J.B. Goodenough, Y. Kim, *Chem. Mater.* 22 (2010) 587–603.
- [2] J.W. Fergus, *J. Power Sources* 195 (4) (2010) 939–954.
- [3] Q. Zhong, A. Banakdarpour, M. Zhang, Y. Gao, J.R. Dahn, *J. Electrochem. Soc.* 144 (1997) 205–213.
- [4] S. Patoux, L. Sannier, H. Lignier, Y. Reynier, C. Bourbon, S. Jouanneau, F.L. Cras, S. Martinet, *Electrochim. Acta* 53 (2008) 4137–4145.
- [5] L. Wang, H. Li, X. Huang, E. Baudrin, *Solid State Ionics* 193 (1) (2011) 32–38.
- [6] J.-H. Kim, S.-T. Myung, C.S. Yoon, S.G. Kang, Y.-K. Sun, *Chem. Mater.* 16 (2004) 906–914.
- [7] D. Li, A. Ito, K. Kobayakawa, H. Noguchi, Y. Sato, *Electrochim. Acta* 52 (2007) 1919–1924.
- [8] K. Takahashi, M. Saitoh, M. Sano, M. Fujita, K. Kifune, *J. Electrochem. Soc.* 151 (2004) A173–A177.
- [9] K.M. Shaju, P. Bruce, *Dalton Trans.* (2008) 5471–5475.
- [10] J. Song, D.W. Shin, Y. Lu, C.D. Amos, A. Manthiram, J.B. Goodenough, *Chem. Mater.* 24 (15) (2012) 3101–3109.
- [11] D. Pasero, N. Reeves, V. Pralong, A.R. West, *J. Electrochem. Soc.* 155 (2008) A282–A291.
- [12] Y. Xia, T. Sakai, T. Fujieda, X.Q. Yang, X. Sun, Z.F. Ma, J. Mcbreen, M. Yoshio, *J. Electrochem. Soc.* 148 (7) (2001) A723–A729.
- [13] N. Amdouni, K. Zaghib, F. Gendron, A. Mauger, C.M. Julien, J. Magn. Magn. Mater. 309 (2007) 100–105.
- [14] M. Kunduraci, J.F. Al-Sharab, G.G. Amatucci, *Chem. Mater.* 18 (2006) 3585–3592.
- [15] M. Kunduraci, G.G. Amatucci, *J. Electrochem. Soc.* 153 (7) (2006) A1345–A1352.
- [16] H. Duncan, D. Duguay, Y. Abu-Lebdeh, I.J. Davidson, *J. Electrochem. Soc.* 158 (5) (2011) A537–A545.
- [17] D. Aurbach, B. Markovsky, Y. Talyossef, G. Salitra, H.-J. Kim, S. Choi, *J. Power Sources* 162 (2) (2006) 780–789.
- [18] F. Sauvage, E. Baudrin, L. Gengembre, J.-M. Tarascon, *Solid State Ionics* 176 (2005) 1869–1876.
- [19] J. Sun, K. Tang, X. Yu, H. Li, X. Huang, *Thin Solid Films* 517 (2009) 2618–2622.
- [20] C. Legrand, L. Dupont, C. Davoisne, F. Le Marrec, J. Perrière, E. Baudrin, *J. Solid State Chem.* 184 (2011) 351–356.
- [21] O. Maqueda, F. Sauvage, L. Laffont, M.L. Martinez-Sarrion, L. Mestres, E. Baudrin, *Thin Solid Films* 516 (8) (2008) 1651–1655.
- [22] H. Xia, S.B. Tang, L. Lu, Y.S. Meng, G. Ceder, *Electrochim. Acta* 52 (2007) 2822–2828.
- [23] H. Xia, L. Lu, *Phys. Scr. T129* (2007) 43–48.
- [24] H. Xia, Y.S. Meng, L. Lu, G. Ceder, *J. Electrochem. Soc.* 158 (8) (2007) A737–A743.
- [25] J. Rodríguez-Carvajal, *Phys. B* 192 (1992) 55. For a more recent version see Rodríguez-Carvajal, *J. CPD Newsletter* 2001, 26, 12, available at: <http://journals.iucr.org/iucr-top/comm/cpd/Newsletters/>. The program and documentation are available at: <http://www.ill.fr/dif/Soft/fp>.
- [26] P. Thompson, D.E. Cox, J.B. Hastings, *J. Appl. Crystallogr.* 20 (1987) 79–83.
- [27] R.D. Shannon, *Acta Crystallogr. Sect. A* 32 (1976) 751–767.
- [28] J.-M. Tarascon, W.R. McKinnon, F. Coowar, T.N. Bowmer, G. Amatucci, D. Guyomard, *J. Electrochem. Soc.* 141 (1994) 1421–1431.